CCFE
CULHAM CENTRE FOR FUSION ENERGY

UK Atomic Energy Authority

UKAEA-CCFE-PR(26)03

Zhiwei Hu, Qigui Yang, Jintong Wu, Duc Nguyen-Manh, M. Yu. Lavrentiev, Pierre Desgardin, Jérôme Joseph, Marie-France Barthe

Quantitative Assessment of Vacancy Defect Populations in Self-Ion Irradiated Molybdenum

Quantitative Assessment of Vacancy Defect Populations in Self-Ion Irradiated Molybdenum

Zhiwei Hu, Qigui Yang, Jintong Wu, Duc Nguyen-Manh, M. Yu. Lavrentiev, Pierre Desgardin, Jérôme Joseph, Marie-France Barthe

This is a preprint of a paper submitted for publication in Nuclear Fusion

Quantitative Assessment of Vacancy Defect Populations in Self-Ion Irradiated Molybdenum

Zhiwei Hu [a, e], *Qigui Yang* [c], *Jintong Wu*[d], *Duc Nguyen-Manh* [b], *M. Yu. Lavrentiev* [b], *Pierre Desgardin* [a], *Jérôme Joseph* [a], *Marie-France Barthe* [a, *]

[a] CEMHTI, CNRS, UPR3079, University of Orléans, F-45071 Orléans, France

[b] UK Atomic Energy Authority, CCFE, Culham Science Centre, Abingdon, Oxon, OX14 3DB, United Kingdom

[c] Institute of High Energy Physics, CAS, 100049 Beijing, China

[d] Department of Physics, Post-office box 43, FIN-00014 University of Helsinki, Finland

[e] Institute of Radiation Physics, Helmholtz Center Dresden-Rossendorf, 01328 Dresden, Germany

Abstract

Microstructural evolution–driven degradation governs material properties and is closely linked with defect behavior. Quantitatively characterizing defects and their evolution is essential for elucidating the underlying degradation mechanisms. To this end, the defects were introduced at room temperature using self-ion irradiation for damage levels ranging from 0.01 to 2 displacements-per-atom. The depth distribution of vacancy defects were characterized by means of a variable-energy positron beam and compared with simulation results. Quantitative analyses of vacancy in the most damaged regions were carried out by combining positron annihilation spectroscopy with a simulated annealing algorithm parametrized with a positron trapping model and first-principles calculations. The defect size distribution -from single vacancy to vacancy clusters- was assessed at each damage levels, providing insights into the quantification of early-stage vacancy defects. Our results revealed that at 0.01 dpa, nearly all vacacncy defect exists as isolated single vacancies. The proportion of isolate single vacancies gradually drops to ~20% with increasing damage level, reaching a steady state (> 0.5 dpa). Meanwhile, clusters consisting of four or more single vacancies account for ~12 % of the total vacancy defects. when the damage level exceeds 0.1 dpa, the formation of large clusters containing more than 15 vacancies, although limited to less than 1% in population, cannot be

excluded. Furthermore, the estimated vacancy accumulation trend is consistent with available computational results, and unveils that the vacancy clustering is more pronounced in molybdenum than in tungsten et the early stage evolution.

Keywords: Vacancy quantification, Defect distribution, Positron annihilation spectroscopy, First-principles calculation, Fusion materials,

1. Introduction

Future fusion power plants require high-performance materials. Tungsten (W) and Molybdenum (Mo) are the most auspicious candidates for plasma-facing components (PFC) [1,2] thanks to their high melting points, thermal conductivity, and low sputtering yield [3]. Compared to W, Mo offers advantages in certain properties and has been chosen to line the inner wall of the Experimental Advanced Superconducting Tokamak (EAST) [4]. For example, radiation-induced activation is lower in Mo than in W [5], and Mo is simpler to manufacture into lighter components than W components. In the operation of the future reactor, monitoring the stability of the plasma is essential. To achieve this, the plasma mirror (PM), as a part of the optical diagnostics system, is used to reflect the light from the plasmas [4]. Promising results [5–7] have been revealed using Mo as PM. Moreover, in tokamaks, inner walls and structural materials are subjected to hydrogen (H) and helium (He) plasma and neutron irradiation, which degrade their properties. Recent research conducted by Lavrentiev et al. [8] demonstrates that the reflectivity of Mo remains stable up to fluences of 10^{18} m^{-2} under self-ion irradiation. In this study, the irradiated Mo samples were characterized by Thermal desorption spectrometry after exposure to deuterium plasma. The deuterium inventory increased with the damage level until reaching a saturation, similar to findings in previous work on W [9]. According to modeling, this saturation occurs when the damage dose reaches 0.5 dpa [10]. This saturation reveals that a steady-state microstructure forms once the damage reaches a certain threshold level [9,11]. This is probably due to competition between Frenkel-Pairs (FPs) recombination, cascades

overlapping [12], and agglomeration of self-interstitial loops, accompanied by the shrinkage of the vacancy clusters [13]. The resulting steady-state microstructure consists of vacancy defects, including single vacancy (V_1) and vacancy clusters (V_n), dispersed within a network of dislocations formed by self-interstitial atoms (SIAs). Both interstitial and vacancy defects capture H and He isotopes, particularly the vacancy defects [14,15]. Furthermore, light-element impurities (LEs) also influence defect evolution [16–19] and serve as potential traps for H [20]. The interaction of H and He with the defects has been observed to cause blistering [21–23], bubbles [24,25], and fuzzy surfaces [17]. The trapping properties of H and He in vacancy defects are a major parameter in the degradation of material properties [26–30], and the kinetic appearance of bubbles and blisters depends on the nature of the vacancy [15,20,31,32]. Therefore, quantifying defects is a crucial step in predicting tritium retention, swelling and material evolution in tokamaks.

Positron annihilation spectroscopy (PAS) is renowned for nondestructive technique to characterize atomic-scale vacancy defects, thanks to its unique sensitivity. For instance, Lhuillier et al. [33,34] and Debelle et al. [35] have identified the signal of the V_1 in W and monitored its evolution with a post-irradiation isochronal annealing experiment. They have observed the activation temperature for V_1 between 523 and 573 K [35]. Positron annihilation is primarily implemented in two types of spectroscopy: Doppler broadening spectrometry and positron annihilation lifetime spectroscopy (PALS), which allow the measurement of two annihilation characteristics: the momentum distribution of annihilated positron-electron (e^+-e^-) pairs and lifetime, respectively [36]. Theoretically, each type of vacancy defect exhibits specific annihilation characteristics, difficult to determine all of them through experimental methods. For this issue, first-principles calculations can provide helpful information [37,38]. Recently, Yang et al. [39] have shown the accurate calculation of the Doppler Broadening Spectrum (DBS) and the lifetime of several transition metals using the two-component density functional theory

(TCDFT) developed by Makkonen et al. [40]. In tungsten, the evolution of annihilation characteristics for different types of vacancy defects from V_1 to the vacancy cluster has been revealed by calculation and experiment [41]. Considering the similarities between W and Mo, we used this first-principles method to calculate the DBS and the lifetime of the vacancy defects in Mo. This method enables the determination of the positron annihilation characteristics (lifetime, ***S***, and ***W***) for vacancy defects that are challenging to isolate and quantify experimentally. In line with the simulation, we employed Doppler Broadening spectrometry with a variable monoenergetic positron beam to characterize the radiation-induced defects in Mo using self-ion at Room Temperature (RT). Furthermore, we conducted the method recently proposed in [42] for qualifying the proportion of each type of vacancy defect from DBS by combining a simulated annealing algorithm, parametrized with a positron trapping model and first-principles calculations. The estimated vacancy defect distribution was compared to Object Kinetic Monte Carlo (OKMC) simulations [43].

2. Methods

2.1 Sample preparation and irradiations

Polycrystalline Mo samples were polished until a mirror-like surface and then annealed at 1200 °C for 2 h. The prepared Mo samples were damaged using 1 MeV self-ion at RT with various fluences, ranging from 2.1×10^{16} to 4.2×10^{18} m^{-2}. The program Stopping and Range of Ions in Matter (SRIM) was used to compute the damage profile, with the 'Kinchin-Pease quick calculation' option recommended by Stoller et al. [44] and recently checked by Lin et al. [45]. The damaged region was predicted between 0 and 400 nm, with the peak at around 110 nm. Tab.1 summarizes the irradiation conditions. 34 eV was used as the threshold displacement energy (TDE) [46]. The fluences used in this work induced maximum damage, quantified in displacement per atom (dpa), ranging from ~0.01 dpa up to ~2 dpa. Further details on preparation and irradiation have been reported in [8].

Tab 1: irradiation conditions for 1 MeV-Mo in Mo using SRIM-2008 Kinchin-Pease quick calculation with a TDE of 34 eV

Fluence (cm^{-2})	2.1×10^{12}	2.1×10^{13}	6.3×10^{13}	1.1×10^{14}	2.1×10^{14}	4.2×10^{14}
Damage (dpa)	0.0096 (~0.01)	0.096 (~0.1)	0.29 (~0.30)	0.48 (~0.5)	0.96 (~1)	1.92 (~2)
Time (s)	64	143	927	2109	2394	5543

2.2 Positron annihilation spectroscopy

Thermalized positrons diffuse in the crystalline lattice and can move to a relatively low electronic density position due to repulsion from the host nucleus. They eventually annihilate with a surrounding electron, emitting two gamma rays of $511 \pm \Delta E$ keV. The energy deviation ΔE depends essentially on the kinetic momentum of the annihilating electron. The gamma rays from the annihilation, are collected in the measured DBS centered at 511 keV, representing the momentum distribution of the annihilated positron-electron pairs starting at 0 m_0c (m_0: electron mass, and c: light speed). The low (resp. high) momentum parameter ***S*** (resp. ***W***) corresponds to the ratio of the counts in the low (resp. high) momentum region over the counts in the total momentum range.

At CEMHTI Laboratory, a DB Spectrometer is coupled to a Slow Positron Beam (SPB-DBS) that produces a monoenergetic positron beam with a variable energy ranging from 0.5 to 25 keV [47]. Annihilation gamma rays are recorded using a high-purity germanium detector with an efficiency of over 25 % at 1.33 MeV. The spectrometer has a dead time of around 10 % and an energy resolution of ~1.25 keV (full width at half maximum, FWHM), equivalent to a momentum resolution of 4.89×10^{-3} m_0c. The ***S*** (resp. ***W***) parameter is calculated in the momentum range of $|2.64| \times 10^{-3}$ m_0c (resp. $(|9.80| - |24.88|) \times 10^{-3}$ m_0c) of each DBS. According to the Makhovian model [48], the maximum penetration of slow positrons in Mo is about 1300 nm. The VEPFIT program [49,50] is used to extract the depth distribution of defects from the ***S*** and ***W*** values measured as functions of positron energy (***S(E)*** and ***W(E)***) by modeling the sample as several homogenous layers. Each layer has specific annihilation characteristics,

including the $\boldsymbol{S}$, $\boldsymbol{W}$ parameters and an effective diffusion length of the positrons, i.e. L_{eff}^{+}. The L_{eff}^{+} is physically related to the concentration of defects which impede the positron diffusion and to the intrinsic diffusion coefficient of positrons D^{+}, which is of about 1.2(1) × 10^{-4} $m^2.s^{-1}$ at 300 K in Mo [51].

$$L_{eff}^{+} = \sqrt{\frac{D^{+}}{\lambda_L + k_{tot}}} \quad (1)$$

Where λ_L is the defect-free Lattice annihilation rate, and k_{tot} the total trapping rate. λ_L, is the inverse of the Lattice positron lifetime τ_L, which means the lifetime of positrons annihilating as delocalized in the perfect lattice. For Mo, τ_L was estimated experimentally and by calculation at values of 103 ps [52] and 106 ps [39], respectively. These values are close to those of tungsten of about 105 ps [41,52,53]. In a solid containing p types of vacancy defects (V_i), positrons can annihilate as delocalized in the perfect lattice and as being trapped in the different defects V_i, with a trapping rate k_i. The measured $\boldsymbol{S}$ and $\boldsymbol{W}$ parameters can be represented as a weighted sum of the specific $\boldsymbol{S}$ and $\boldsymbol{W}$ values associated with each type of annihilation state j (i.e. p defects and lattice) and their respective annihilation fractions (f_j), using a trapping model [36] with p+1 states. The f_i for individual potential defects i are given by the following expression:

$$f_i = \frac{k_i}{\lambda_L + k_{tot}} \quad (2)$$

The vacancy concentration C_i relates to the specific positron trapping coefficient μ_i and the trapping rate k_i, expressed as $C_i = k_i/\mu_i$. In W, the specific trapping coefficient of V_1 is about (6 ± 3) × 10^{15} $m^3.s^{-1}$ [36,54] and should be equivalent in Mo due to similar crystalline structure and lattice parameters in both materials. For small vacancy clusters containing less than ten V_1, their specific trapping coefficients are proportional to the number n of the included V_1, i.e. $\mu_{V_n} = n \cdot \mu_{V_1}$ [36]. On the other hand, for the large vacancy clusters containing more than 10 V_1, the estimation of specific trapping coefficients was detailed in [55].

149 ### 2.3 First-principles calculations

150 The first-principles calculations were conducted by using the Vienna *Ab initio* Simulation
151 Package (VASP) [56] with the projector augmented wave (PAW) method [57]. The generalized
152 gradient approximation with the Perdew-Burke-Ernzerhof exchange-correlation function[58]
153 was used for the electron exchange and correlation energy. The 6 × 6 × 6 bcc supercells
154 containing 432 lattice sites were used for all calculations. The plane-wave cutoff energy was
155 set to 230 eV, and the Γ point only was used for all calculations. We chose the PAW potential,
156 which treats the $4p^6 4d^5 5s^1$ electrons as valence states in Mo. The convergence criterion for the
157 electronic loop was 10^{-5} eV. The force tolerance for ionic relaxation was 0.01 eV/Å. Hou et al.
158 [59] have determined the stable structures of vacancy clusters by minimizing their Wigner-Seitz
159 areas, the same structures of vacancy clusters were used in this study. Because for a give
160 vacancy cluster in bcc metals, the configuration with minimum Wigner-Seitz area is always the
161 same, regardless of the type of materials.

162 After the standard DFT calculations, the positronic structures were computed based on the
163 electronic structures computed by two-component DFT [60]. The Rubaszek weighted-density
164 approximation (WDA) [61] was used for the e^+-e^- correlation potential to compute the positron
165 densities. The positron implementation was developed and provided by Makkonen et al. [40],
166 and the WDA part was developed by Callewaert et al. [62]. A detailed discussion about using
167 WDA to compute the positron annihilation characteristics in vacancy clusters can be found in
168 Ref. [41]. The positron was approximated not to affect the average electron density, and the
169 zero-positron-density limit was used [60]. Although the zero-density-limit results in the non-
170 self-consistent treatment of positron densities, it has been shown in Ref. [34] that the non-self-
171 consistent calculation yields very similar results with the fully self-consistent calculations for
172 small vacancy defects. The momentum distribution of annihilating e^+-e^- pairs (Doppler spectra)
173 was computed with the state-dependent scheme [63] and PAW method [40]. All computed

Doppler spectra were convoluted with a Gaussian function with a FWHM corresponding to the experimental resolution (4.89×10^{-3} m_0c).

3. Results

3.1 First-principles calculation

In our previous work [41], the two-component DFT was used to calculate the annihilation characteristics of several annihilation states in W. The evolution from the ***Lattice*** to V_1 and from V_1 to the largest vacancy cluster (V_N) was demonstrated in agreement with the experiment [41]. Accordingly, the two-component DFT was also employed to calculate *annihilation characteristics* (lifetime and ***S, W*** parameter) of various annihilation states (Lattice and vacancies) in Mo with identical parameters [41]. The line L_1 connects the ***Lattice*** and V_1, ***S***, ***W*** points corresponding to the annihilation between these two states with different fractions.

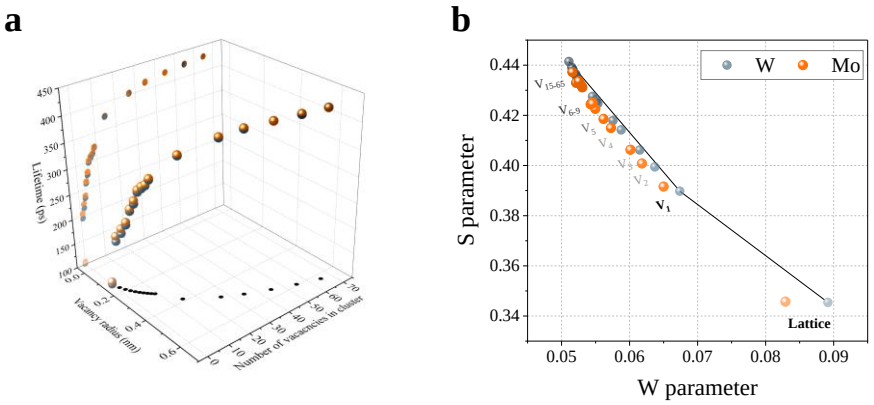

Fig. 1: two-component DFT-calculated a) positron annihilation lifetime and b) momentum parameters S vs W curves for Mo and W [41]*: the vacancy radius was estimated assuming a spherical model.*

Fig. 1 compares the positron annihilation characteristics of vacancy clusters in tungsten and molybdenum (positron lifetimes a and ***S-W*** plot b). Fig. 1a clearly shows that, with the increase of vacancy cluster size (from V_1 to V_{20}), the positron lifetime gradually increases from 200 ps to 350 ps. Fig. 1b presents the ***S-W*** points of vacancy clusters in W and Mo. The ***S-W***

points follow the same trend with the increase of vacancy cluster sizes. However, when the vacancy cluster size is greater than V_{27} (radius = 0.47 nm), the positron annihilation characteristics reach saturation, in this regime, the identifiable largest vacancy cluster is referred to V_N. When comparing the difference in the ***W*** parameter between Mo and W for the various annihilation states, the values for the ***Lattice*** are the most remarkable. The ***W*** is lower in Mo than in W, probably because the number of electrons close to the nuclei (core electrons) is higher for W. The ***S*** parameter which mainly reveals the annihilation of the valence electrons, is very close in both Mo and W. In addition, it should be noted that in the experimental spectra, the high momentum region has relatively low counts, making it challenging to highlight the difference in the ***W*** parameter, as shown in supplementary II.

3.2 Positron annihilation spectroscopy

3.2.1 Reference sample

The ***S(E)*** curve of the Mo reference sample annealed at 1200 °C for 2h is plotted in Fig. 2a, the data was adequately fitted using VEPFIT in the one homogenous layer model. The annihilation characteristics were $\boldsymbol{S_{Ref}}$ = 0.377 (3), $\boldsymbol{W_{Ref}}$ = 0.079 (2), and the $\boldsymbol{L_{eff}^{+}}$ of positrons equals 63 nm. The fitting (Tab.1) was carried out from 2 keV, as the annihilation fraction at the sample surface is important below this energy [41]. As the $\boldsymbol{L_{eff}^{+}}$ is shorter than the intrinsic diffusion length (110 nm) determined at 300 K for Mo [48], this suggests that a small fraction of vacancy defects were not eliminated during the annealing process.

After a further annealing at higher temperature of about 1700 °C/2h under high vaccum (10^{-5} Pa), the $\boldsymbol{L_{eff}^{+}}$ expands to 92 (18) nm, and the annihilation characteristics $\boldsymbol{S_{1700}}$ and $\boldsymbol{W_{1700}}$ (blue circle) overlap with the ***Lattice*** point in W (see the ***S-W*** curve in Fig. 2b), suggesting that the ***Lattice*** annihilation characteristics $\boldsymbol{S_L}$(Mo) and $\boldsymbol{W_L}$(Mo) for Mo are very close to those experimentally determined in W. This confirms the suggestion in the part 3.1, i.e. the ***S***, ***W*** parameters corresponding to ***Lattice*** and V_1 are very close for Mo and W.

In Fig. 2b, the ***S, W*** points extracted from ***S(E)*** and ***W(E)*** using VEPFIT for Mo samples are plotted with the Lattice, V_1, and V_N points already determined for W [33,54,64]. The specific point (dark circle in Fig. 2b) of the reference Mo sample ($\boldsymbol{W_{ref}}$, $\boldsymbol{S_{ref}}$) is aligned on the V_1 line found in W and is located slightly at a higher left position on this line relative to the W ***Lattice*** point (red star in Fig. 2b). Furthermore, considering that defects are mostly V_1, the residual defects concentration were calculated using equation (4) in literature [9] with the lifetime of the Mo Lattice of 103 ps [52]. The remaining vacancy concentration is about 3×10^{24} m^{-3} in the reference sample with a $\boldsymbol{L_{eff}^{+}}$ of about 63 nm, and 5.5×10^{23} m^{-3} in the reannealed Mo sample with a $\boldsymbol{L_{eff}^{+}}$ of 92 nm. It is important to note that, after the initial annealing at 1200 °C for 2 hours, the remaining concentration of vacancy defects is too low to interfere with the study of irradiation-induced defects. This previous state before irradiation is named refrerence state i.e. *Ref* in the following discussion.

3.2.2 Self-irradiated samples

The ***S(E)*** curves plotted in Fig. 2a, reveal the distribution of defects in Mo samples irradiated at fluence in the range from 2.1×10^{16} to 4.2×10^{18} m^{-2}. The ***S(E)*** curves have similar shapes for all fluences. ***S*** increases from the approximately identical value measured at 0.5 keV up to a maximum obtained as positron energy increases with fluence. Thereafter, ***S*** decreases towards, but does not reach, the value in the reference sample $\boldsymbol{S_{Ref}}$. The ***S*** parameter discloses the size and/or concentration of open volume where e^+-e^- pairs were annihilated. As the fluence increases, the ***S*** parameter increases, indicating the detection of a larger size and/or higher concentration of vacancy defects. However, the increase slows down when the fluence exceeds 6.3×10^{17} m^{-2}. For the highly damaged region (***E***<10 keV), the ***S(E)*** curves almost overlapped, and ***W(E)*** curves exhibited a mirror evolution, suggesting that the defect distribution probably saturates. The ***S(E)*** and ***W(E)*** curves can be fitted using the VEPFIT program [15,16] by

describing the samples in three homogeneous layers. The fitted *annihilation characteristics* in Layers 1, and 2 are summarized in Tab.2.

*Tab. 2: Annihilation characteristics $S_{Lay(i)}$, $W_{Lay(i)}$, and $L+_{Lay(i)}$ for layers i = 1,2, extracted from the fitting of the **S(E)** and **W(E)** curves with the VEPFIT program using a three-layer model for samples irradiated at different fluences, ranging from 2.1 × 10^{16} to 4.2 × 10^{18} m^{-2}. The corresponding peak damage value ranges from 0.01 to 2 dpa. R is the slope of the straight line connecting point (S_{lay1}, W_{lay1}) and the Lattice point in the S-W curve, i.e. $R=(S_{lay1}-S_L)/(W_{lay1}-W_L)$. The Layer boundary (Lb) is the depth from the sample surface at which each layer expands. The annihilation characteristics of Layer III are fixed to those of the reference sample (S_{lay3} = 0.377 (5), W_{lay3}=0.079 (2), and L^{+}_{lay3} = 63 nm). Surface annihilation characteristics are equivalent (S_{surf} = **0.400 (5)**, W_{surf} = **0.065 (3)**) for all samples. The incertitude of the fitted value is about 0.004 and 0.002 for S and W, respectively.*

Damage	Layer 1					Layer 2				
dpa	S_{lay1}	W_{lay1}	R	L_{lay1}^{eff+}	Lb (nm)	S_{lay2}	W_{lay2}	R	L_{lay2}^{eff+}	Lb(nm)
~0.01	0.421	0.057	2.05 (16)	14 (4)	200 (9)	0.399	0.069	2.08 (28)	50	716 (31)
~0.1	0.440	0.051	2.18 (10)	13 (2)	252 (9)	0.412	0.062	2.05 (15)	40	856 (33)
~0.3	0.448	0.049	2.25 (10)	12 (2)	227 (11)	0.424	0.057	2.08 (12)	35	865 (27)
~0.5	0.449	0.048	2.27 (9)	11 (2)	260 (13)	0.427	0.056	2.11 (12)	30	937 (27)
~1	0.451	0.047	2.27 (9)	10 (2)	311 (15)	0.427	0.056	2.07 (11)	30	945 (29)
~2	0.451	0.047	2.27 (9)	10 (2)	356 (19)	0.429	0.055	2.11 (11)	30	1000 (36)

Fig. 2c shows the evolution of the S parameter as a function of depth for each fluence. The first two layers displayed the damaged region, and the third one was fixed with annihilation characteristics of the reference sample (S_{ref}, W_{ref}, and L_{eff}^{+} = 63 nm). In addition, the L_{eff}^{+} in each layer is shown in Fig. 2d as a complement of the S parameter. The thickness of the first layer, L_b, and the effective positron diffusion L_{eff}^{+} vary from 200 to around 356 nm, and from 10 to 17 nm, respectively. The fit confirms the damage profile predicted using the SRIM program, with the highest S and the shortest L_{eff}^{+} found in Layer 1 for each sample. This suggests that most irradiation-induced defects are located in the first 300 nm. Thus, the fitted S, W value in Layer 1, i.e. S_{lay1} as a function of W_{lay1} were plotted in Fig. 2b. The slope R of the straight line connecting each specific S-W point (W_{lay1}, S_{lay1}) to the ***Lattice*** point (W_L, S_L), calculated as the ratio $(S_{lay1}-S_L)/(W_{lay1}-W_L)$, reflects the evolution of the defect size.

At the lowest fluence (2.1 × 10^{16} m^{-2}), the width of Layer 1 is around 200 (9) nm. Compared to the reference sample, L_{eff}^{+} has decreased by more than 30 %, from 63 nm to around 17 (2) nm, due to the positron trapping in irradiation-induced defects. In addition, the fitted values

263 $\boldsymbol{S_{lay1}}$ =0.421(4), and $\boldsymbol{W_{lay1}}$ = 0.058(2) are close to those of V_1 experimentally determined in W
264 (the green crossed circle in Fig. 2b), but slightly further to the right. The corresponding slope
265 $\boldsymbol{R}$ is 2.05(16), which is slightly larger than that of the V_1 line in W (1.85(3) [9]). These results
266 indicate that V_1 is a dominant trap for positrons, although it cannot be ruled out that a small
267 fraction of positrons probably annihilate in vacancy clusters. In Layer 2, from 200 (12) to 716
268 (31) nm, $\boldsymbol{S_{lay2}}$ is lower than $\boldsymbol{S_{lay1}}$, and the $\boldsymbol{L_{eff}^{+}}$ is about 50 nm. Although the irradiations still
269 induced defects in this layer, their concentration is considerably lower than in Layer 1, and
270 annihilation in the ***Lattice*** becomes significant as the $\boldsymbol{L_{eff}^{+}}$ lengthens.

271 The $\boldsymbol{S}$ and $\boldsymbol{W}$ parameters of the vacancy clusters (V_2-V_{55}) in W were also plotted in Fig. 2b.
272 Their values were transposed in the experimental frame network from theoretical values using
273 the experimental and theoretical V_1-V_N lines as the references [55]. As the fluence increases,
274 the fitted annihilation characteristics in Layer 1 vary following defect size evolution. Once the
275 peak damage dose has reached around 0.5 dpa, the thickness of the Layer 1 extends to about
276 260 nm, and the variation of annihilation characteristics is discontinued (Tab.1). The $\boldsymbol{S}$ *(resp.*$\boldsymbol{W}$*)*
277 parameter converges around 0.451 (resp. 0.047). The $\boldsymbol{R}$ ratio reaches the value 2.27 (9), and the
278 $\boldsymbol{S}$, $\boldsymbol{W}$ points are located between the $\boldsymbol{S}$,$\boldsymbol{W}$ points corresponding to the clusters V_3 and V_4 (Fig.
279 2c), revealing the formation of small vacancy clusters. At the same time, the $\boldsymbol{L_{eff}^{+}}$ shortened to
280 about 10 nm (Fig. 2d), showing the increase of the positron trapping rate. For a damage dose
281 greater than 0.5 dpa, the $\boldsymbol{S}$-$\boldsymbol{W}$ points for Layer 1 remain almost superimposed, indicating that
282 the defect distribution reaches a steady state in the first 350 nm in the sample. A similar
283 saturation effect was already observed in W self-ion irradiated at RT [9,11]. The saturation
284 point for W is plotted in the cyan sphere in Fig. 2c [9]. Remarkably, the saturation $\boldsymbol{S}$ (resp. $\boldsymbol{W}$)
285 parameter is higher (resp. lower) in Mo than in W, suggesting that the proportion of the vacancy
286 clusters is higher in Mo than in W.

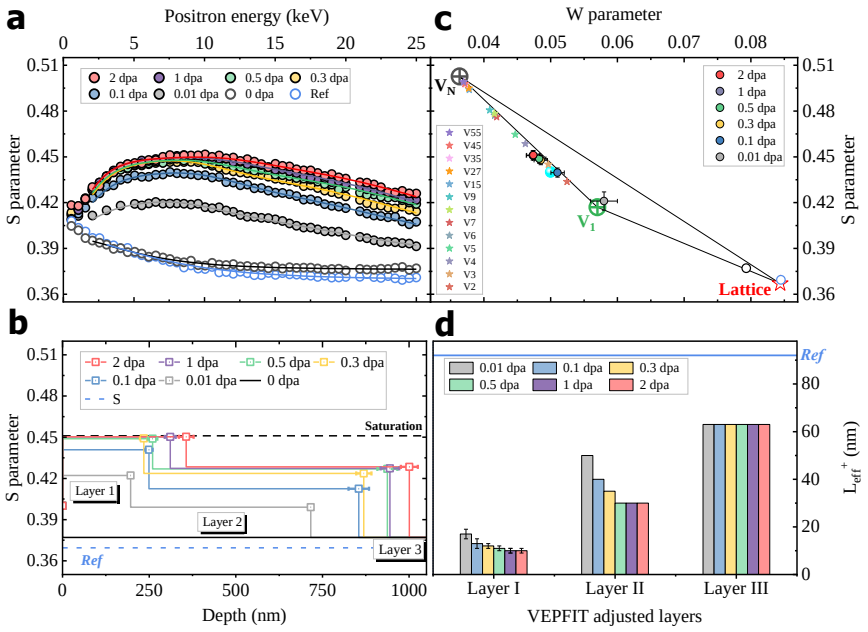

Fig. 2: Annihilation characteritics in Mo samples before and after self-irradition: a) S parameter as a function of positron energy E, b) depth profile of parameter S extracted for the first layer from the S(E) and W(E) using VEPFIT; c) S-W plot of the S and W extracted for the first layer in the reference annihilation characteristics of Lattice (open red star), single vacancy (green crossed-circle) and saturation signal V_N (dark crossed circle) determined in W[33,35,64], the colored solid stars represent the estimated S,W for various vacancy clusters. The cyan point corresponds to the steady-state obtained in self-irradiated W [9] d) positron effective diffusion length (L_{eff}^{+}) in adjusted layers using VEPFIT program.

In addition, deeper damage was created with increasing fluence (as shown in Fig. 2c), extending much deeper than the 300 nm depth predicted by the SRIM simulation for Mo irradiated with 1 MeV self-ions [8]. A similar result has been observed by He et al.[65] in the case of implantation of yttrium, titanium, and oxygen in Fe. This difference is due to the channeling effect in the polycrystalline sample with large grain size (> 50 µm), which is not considered in the SRIM calculations.

4. Discussion

4.1 Quantitative evaluation of defect size distribution

Recently, we extracted complete vacancy distributions in self-ion irradiated W, using a quadratic programming and simulated annealing algorithm (SA)[42], parametrized with a

positron trapping model including pure vacancy defects Vi with i=1-65 [55]. The concentration and proportion of each vacancy defect were estimated using the same method in the self-irradiated Mo samples. The results are shown in 3a and b, where clusters containing more than 15 vacancies are not displayed, as their concentration is close to the lower detection limit (Fig. 7 in Supplementary Information) of SPB-DB. For the lowest damage level (0.01 dpa), the estimated proportion of V_1 is 99%, and the concentration reached around 5×10^{25} m^{-3}. This is in line with the first conclusion made in the qualitative interpretation of the experimental results, which established that V_1 is the dominant trap for positrons with a minor proportion of vacancy clusters at the lowest fluence (0.01 dpa).

When the damage escalates from 0.01 to 0.1 dpa, the proportion of V_1 decreases to 48%, and ~40% vacancy clusters account for $V_{2\text{-}3}$, and ~10% for $V_{4\text{-}7}$. Up to the 0.3 - 0.5 dpa, V_1 and $V_{4\text{-}6}$ clusters represent a quarter of the total proportion. Following the damage accumulation until 2 dpa, the concentration of V_1 declined again, and its proportion reduced to about 20 %. At the same time, the concentration and proportion of $V_{4\text{-}9}$ manifestly increased. According to DFT, the V_1 is less monbile at RT, and binding energy is predicted to be negative for V_2, whereas the vacancy clusters can still algomerate in the cascades or the overlapped cascades resulting in large clusters. The larger cluster of 15 vacancies (radius = 0.35 nm) reached the lower limit of the SPB-DB (~ 3×10^{22} m^{-3}, Fig. 3a and Fig.8 in the Supplmenetary information) as the damage level increases) to 0.5 dpa. In addition, each size of vacancy reached a stable level when the damage accumulated at 0.5 dpa or more, agrees with the computational work in case of tungsten [66].

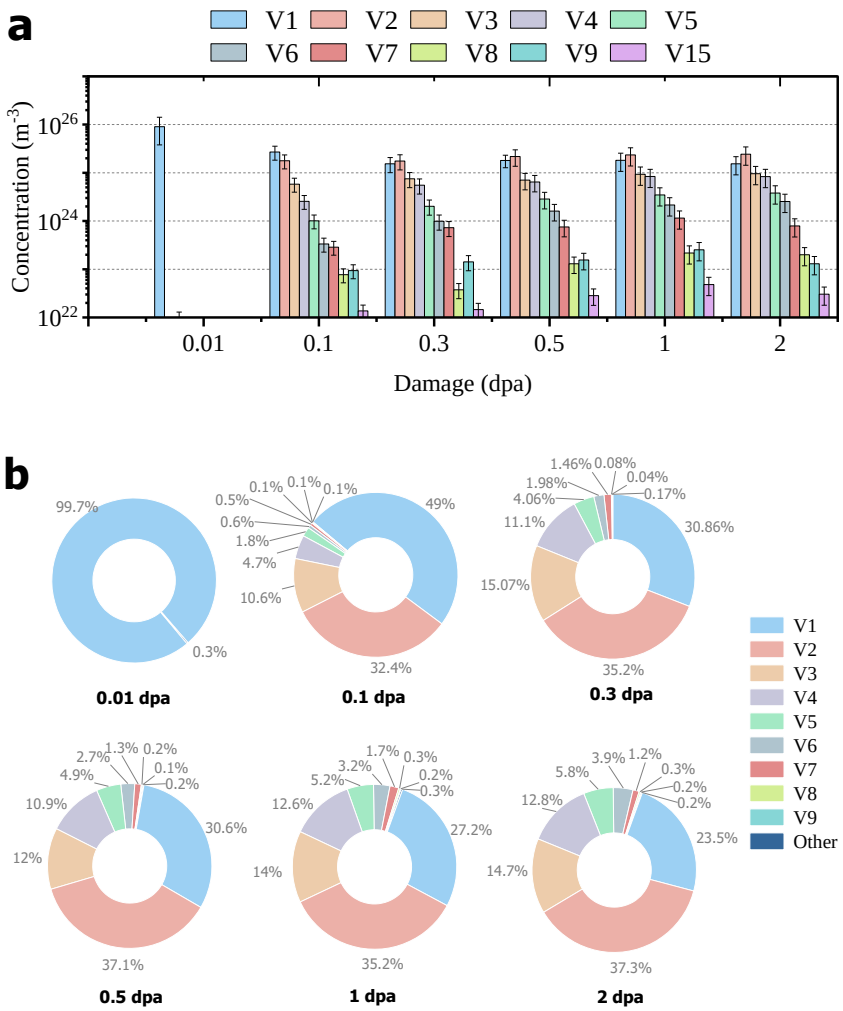

Fig. 3: a) concentration and b) proportion of the vacancy defects probed by positrons in 1MeV self-ion, RT-irradiated Mo in the first ~300 nm below the surface(corresponding to the first layer) for damage levels ranging from 0.01 to 2 dpa (with TDE= 34 eV, SRIM2008-K-P). These values were extracted from the S and W experimental values using the methodoly described in [42]

Selby et al. [67] operated molecular dynamics (MD) to mimic the evolution of the defects at 300 K in Mo. The simulation involved Primary Knock-on Atom (PKA) energies up to 50 keV, whereas 98% PKA have an energy higher than 50 keV according to SRIM with experimental conditions. These simulated results showed over 80 % of vacancies were isolated

single vacancies, and the largest vacancy cluster contained nine vacancies. This result might compare with low fluence experience, in cases where the cascades overlap is less pronounced.

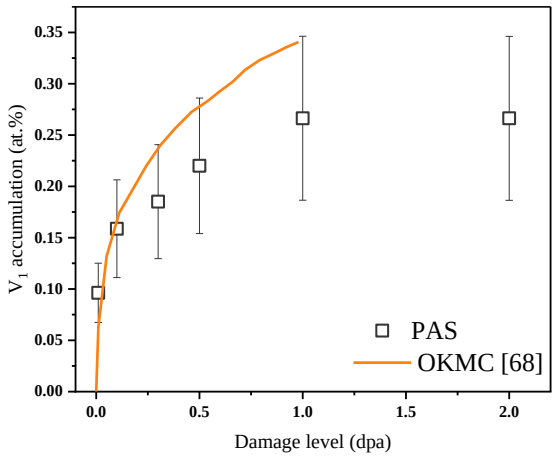

Fig. 4: comparison of estimated V_1 accumulation as a function of the damage level using PAS and OKMC [43], the computational value averages the vacancy concentration value in the first 400 nm, and the experimental data represent the vacancy accumulation in Layer I obtained from the fit, its thickness varies with damage level from 200-356 nm smuurized in Table.2.

Recently, Hou et al. [68] employed OKMC simulation under our irradiation experiments to better align with MD on the damage accumulation time scale with the present experiment. The authors showed that the SIA defects had annihilated quickly with vacancies or at the sample surface. Despite the limited diffusion of vacancies at 300 K, vacancy clusters (> V_6) formed. The authors suggest that such vacancy clusters may form within the core of the cascade due to the high density of vacancies, enabling short-scale agglomeration after diffusion or as a result of cascade overlapping. These results are consistent with the estimated vacancy clusters proportion derived from the PAS data in this study, as illustrated in Fig. 3. Furthermore, the authors observed vacancy depletion at depth beyond 400 nm, correlating well with the decrease in the S parameter shown in Fig.2 (a-c). Fig.4 compares the vacancy accumulation (total concentration of isolated V_1 and those included in the vacancy clusters) as damage increases, based on PAS data and OKMC simulations. Both computational and experimental results reveal

similar trends. In addition, the experimental data reveal that V_1 accumulation reaches saturation when the damage level exceeds 0.5 dpa.

4.2 Steady-state vacancy distribution

Focusing on the vacancy steady state, Fig.5a compares the relative ***S*** parameter, ***S/S$_L$*** (relative ***S*** parameter to Lattice), as it varies with damage accumulation in Mo in the present study and previously reported data in W [9,54,64,69]. A steady-state behavior is observed in both materials, though Mo exhibits a higher S saturation value. Vacancies in both metals accumulate rapidly up to 0.5 dpa, after which their proportion converges. Notably, defect evolution appears to be independent of self-ion energy, as similar trends are observed for 2 and 20 MeV self-ion irradiation in W [9,54,64,69].

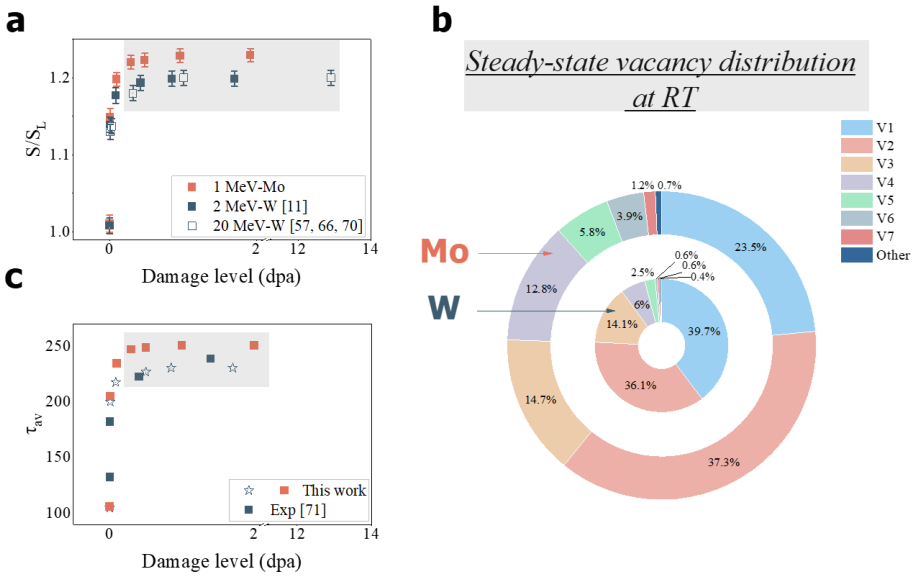

Fig. 5: a) the relative S value, S/S$_L$, and b) the proportion of aggregated vacancies as a function of the damage level caused by self-ion in Mo (1 MeV) and W (2 MeV & 20 MeV) at RT, c) The e$^+$ annihilation lifetime estimated (hollow star) for each damage levels in comparison with experiments [70]

Fig. 5b highlights that, at the defect steady state (> 0.5 dpa), the proportion of vacancies within clusters is significantly higher in Mo (76.5%) compared to W (60%). To further affirm the difference in vacancy proportions between Mo and W, we calculated the averaged lifetime τ_{av} by weighing the lifetime of vacancies (using data in Fig. 1a) with the annihilation fractions determined by SA [55]. Fig. 5c shows the progression of τ_{av} with damage level. For W, the estimated lifetime evolution with damage accumulation coincides with experiments [70], validating the SA method for estimating annihilation fractions. A lifetime of around 231 ps was found for the steady state of defects in W. In comparison, a longer τ_{av} of 250 ps is determined for Mo, consistent with the SPB-DBS results, indicating a higher proportion of large vacancies in Mo since the positron lifetime for each type of vacancy defect are very close in both metals Mo and W (see Fig 7, and Table3 in Supplementary Materials). It is also noteworthy that the binding energy of $V_{2\text{-}3}$ is relatively close to zero for W and slightly negative for Mo, according to references [71–73].

The vacancy size distribution could be strongly affected by the binding and migration of vacancy defects and interstitials. We calculated the binding energies for V_1 to V_9 using DFT calculations (see Fig. S1 in the SI). Notably, the binding energy of V_2-V_3 is near zero for W and slightly negative for Mo, as reported in Refs. [71–73] at 0K. To date, whether V_2-V_3 forms at RT in Mo or W remains unresolved. Only Park et al.[74] reported a binding energy of about 0.7 eV for V_2 in W using Field-ion spectroscopy. Impurity atoms are also known to stabilize V_2 [75,76]. Recently, Zhang et al.[77] estimated the effect of temperature on the binding free energy, finding that the latter increases with rising temperature. Although V_2 remains unstable at RT, two isolated V_1s located at the first nearest-neighbors tend to bind with each other from 700 K, which is an attainable temperature during cascades. Given this, we considered the possibility of the e^+-e^- annihilations in V_2 and V_3. Moreover, it is remarkable that although the cluster containing less than seven V_1 account for 99 % of the total vacancy proportion in both

metals, larger vacancies may also be formed, though in a limited concentration. Quantification of these larger dfects is difficult, as for cluster with more than 15 V_1 fall outside the optimal detection range for the SPB-DBS method, as shown in Fig. 8 in Supplementary I.

The migration energy E^m is the lowest for the self-interstitial atoms (SIA) (Fig.1 in the supplementary). For one-dimensional diffusion in a <111> direction, E^m_{SIA} is about 0.064 eV in Mo and 0.040 eV in W [78]. Thus, the SIA should be very mobile due to their very low migration energy in the Mo and W matrix. For the small vacancies, the tri-vacancy has the lowest E^m in both materials, and for the other vacancy defects V_1, V_2, and V_4, their E^m is lower for the Mo matrix. Hou et al.[43] calculated using DFT, the binding energy for larger clusters containing up to 47 vacancies in Mo. They showed that E^m increases more or less with the number of vacancies in the cluster up to 15, reaching 2 eV and then remaining between 1 and 2 eV. It has to be noted that the probability of dissociation of vacancy clusters is very low at RT. Agglomeration is possible if vacancies can diffuse and link up with each other. Based on the Arrhenius diffusion equation, the distances that V_1 and V_3 can travel at 300 K during the duration of the irradiation at 0.5 dpa (2100 s) are estimated to be about 2×10^{-5} nm and 7.8×10^{-3} nm, respectively. However, the local annealing due to the collision of the ion might enhance their mobility, so the agglomeration of vacancies might occur in the core of cascades, where the density of vacancies is very high, facilitating short-scale diffusion and interactions among vacancies. In addition, vacancy diffusion and binding should be more probable in Mo, given its lower migration energy compared to W. The higher proportion of vacancies within clusters in Mo could, in part, be attributed to the difference in their evolution mechanisms.

On the other hand, De Baker et al. [79] determined the fragmentation energy[1] (E_{fr}) in various materials using MD and Binary Collision Approximation (BCA) simulations. They

[1] The energy above which one cascade can split into several subcascades

found that the number of subcascades increased linearly with the PKA energy when E_{PKA} exceeds E_{fr}, determined to be 17 keV for Mo and 75 keV for W. In bcc metals, cascades overlapping were found to consistently reduce the size of the pre-existing large voids (>100 vacancies) when cascades partially overlap with the defect in W [80] and Fe [13]. In Fe, the size of all clusters -except for the single vacancy- was reduced after a fully overlapping cascade. This reduction depended on PKA energy and interatomic potential but was independent of the initial cluster size [81].

Furthermore, the recombination of FPs in both Mo and W is similar, primarily due to the high mobility of the SIAs. Consequently, the recombination rate of FPs is expected to be comparable in Mo and W, given the equivalent migration energy of SIAs (Fig.1 in the supplementary). However, the TDE in Mo is lower than in W. The arc-dpa model [76] was used to quantify these differences to estimate the average number of FPs produced per cascade. The $b_{arc-dpa}$ and $c_{arc-dpa}$ parameters were taken from Ref. [82]. For Mo, $b_{arc-dpa}$ value was taken from Ref. [83], in which it was suggested that -1 is a proper value for most metals. The $c_{arc-dpa}$ parameter represents the cascade efficiency. According to references [67,84], using classical MD, the cascade efficiency of pure Mo is ~0.2. Therefore, $c_{arc-dpa} = 0.2$ was used. Using the TDE value in Table 4, the arc-dpa model estimated the average number of defects produced in a single cascade event. The results indicate a slightly higher number of created defects in Mo (640 FPs) compared to W (559 FPs).

Tab. 3: related energies to the evolution of defects in W and Mo, E_{fr}: fragmentation energy, over which the cascades could split into several subcascades, TDE: threshold displacement energy, energies are presented in keV, mean: mean PKA energy, equal approximately to a half of the maximum value in the PKA energy predicted by SRIM program. T_d: damage energy kinetic energy available to provoke atomic displacement after losing the electronic ionization energy, kinetic energy available to provoke atomic displacement after removing the electronic ionization energy.

	E_{fr}(keV)	TDE (eV)	T_d (keV)	Number of FPs created in one cascade
Mo	17 [a]	34 [b]	282 [d]	640 [d]
W	75 [a]	55 [c]	600 [d]	559 [d]

[a] reference [79], [b] reference [85], [c] reference [86], [d] reference [87].

The number of vacancies created by a single event of cascades is higher in Mo than in W using the arc-dpa model. After some of these vacancies recombine with SIAs, the remaining vacancies in Mo have a stronger clustering tendency than those in W. In addition, it appears that vacancies in W are less mobile at RT, as indicated by the migration energy presented in Fig.1 in the supplementary. The higher proportion of vacancy clusters in Mo compared to W is likely due to subtle differences in collision cascade overlapping and Frenkel pair recombination between the two materials, resulting in a difference from the early stage of the evolution.

Conclusion

In this study, we combined the PAS, first-principles calculation, and SA algorithm to quantitatively analyze the size distribution of vacancy defects induced by self-ion in Mo and W at RT. The proportion of each vacancy defect from V_1 to V_9 was depicted for the first time based on experimental data, and the primary conclusions have been reached as follows:

(i) Comparable e^+ annihilation characteristics in vacancy clusters in W and Mo: The annihilation characteristics exhibit similar evolution from V_1 to the saturation (V_{35}, ~0.5 nm in radius).

(ii) At low irradiation dose (~0.01 dpa), the predominant defects observed are nearly 100% V_1 in both Mo and W. At 0.3 dpa, the presence of V_{15} (radius = 0.35 nm) becomes detectable by PAS, and the vacancy aggregation rate converges with a damage level of about 0.5 dpa or more. The vacancy accumulation exhibits a trend comparable to that of the OKMC simulation. Alougth the damaged zone detected using SPB-DBS is deeper than thoses OKMC or SRIM estimated, probably due to the channeling effect.

(iii) At the defect steady state (> 0.5 dpa) in Mo, the proportion of V_1 decreases to approximately 20 %. The proportion of V_1 accounted for about 40 % of total vacancies in W, whereas accounting for 23.5 % in Mo, revealing a higher vacancy

clustering tendency in Mo. Each size of the vacancy fraction reached a stable level as predicted by computational work.

These findings will significantly enhance the investigation of vacancy defects in metals. The method enables reliable quantitative analysis of vacancy proportions from primary defect distribution until the steady state at RT, addressing the scarcity of experimental data.

Declaration of Competing Interest

The authors declare that they have no known competing financial interests or personal relationships that could have appeared to influence the work reported in this paper.

Credit authorship contribution statement

Zhiwei Hu: PAS experiments, data processing and interpretation, writing – original draft & editing, ***Qigui Yang***: First-principles calculation, data analysis, writing – original draft & editing, ***Jingtong Wu***: data processing, interpretation, ***Duc Nguyen-Manh & M. Yu. Lavrentiev****: Irradiation experiments* ***Pierre Desgardin****:* Supervision, SPB-DBS experiments ***Jérôme Joseph:*** Sample preparation and technical support, ***Marie-France Barthe***: Conceptualization, validation, data processing and interpretation, writing – review & editing.

Acknowledgments

This work has been carried out within the framework of the EUROfusion Consortium, funded by the European Union via the Euratom Research and Training Program (Grant Agreement No 101052200 — EUROfusion). Views and opinions expressed are however those of the authors only and do not necessarily reflect those of the European Union or the European Commission. Neither the European Union nor the European Commission can be held responsible for them. Qigui Yang acknowledges the financial support by the National Natural Science Foundation of China (Grant No. 12305338). The authors thank Dr. Ilja. Makkonen at

Helsinki University for sharing the positron code. The authors acknowledge Maylise Nastar at CEA for the fruitful discussion.

Supplementary

I. Binding and migration energy of vacancy clusters in Mo and W

Table. 1 summarizes the binding energy E_b of a cluster consisting of n vacancies, V_n, which are calculated as follows :

$$E_b = nE_{V_1} - E_{V_n} - (n-1)E_{\text{lattice}} \quad (1)$$

in which E_{V_1} and E_{V_n} are the energies of supercells with a mono-vacancy and one V_n cluster, respectively. E_{lattice} is the energy of a supercell of perfect lattice. Using the Eq. (1), positive binding energy means attractive interaction and negative binding energy means the opposite. The total binding energy increases with increase number of the V_1 including in the cluster, similar results are found in the Ref. for Mo[88] and for W[73]. The migration energy for vacancy defects from V_1 to V_4 is taken from the references [77-79].

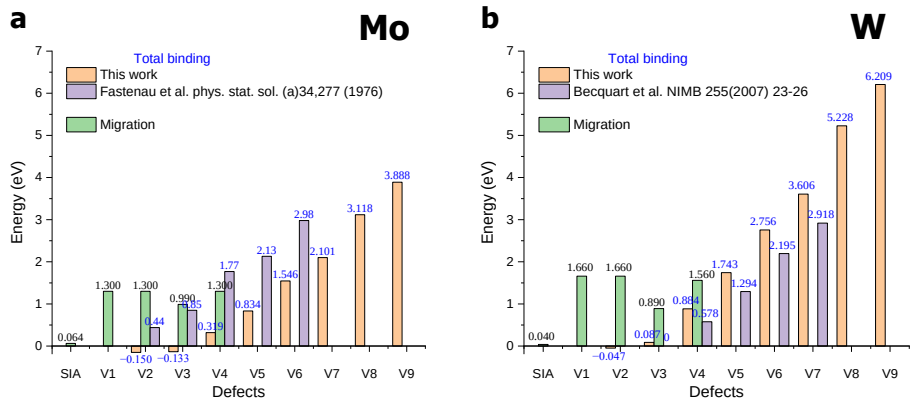

Figure 6: Reported migration energy from V_1 to V_4 in references [77-79], and binding energy of various vacancies with relaxation calculated using DFT in the present work, compared with literature in a) Mo [88] and b) W[73].

II. Sensitivity of the SPB-DBS

After calculating the specific trapping of vacancies, μ_{Vi} as it is explained in [36], we applied a one-trap trapping model for each vacancy. ***S*** parameter can be expressed versus defect concentration C_{Vi} by equation (4):

$$S = \frac{C_{Vi}\mu_{Vi}S_{Vi} + \lambda_L S_L}{C_{Vi}\mu_{Vi} + \lambda_L} \quad (4)$$

where S_{Vi} is the parameter for the vacancy defect Vi as calculated using TCDFT.

Fig. 7 presents the sensitivity of the SPB-DBS to the vacancy concentration in Mo for various vacancy defects from V_1 to V65. When the vacancy concentration is 0, the annihilation fully occurs at the ***Lattice***, the relative ***S*** value, $\boldsymbol{S/S_L}$, equals 1. When the positrons are trapped in vacancies, the $\boldsymbol{S/S_L}$ increases with the vacancy concentration until a specific value which depends on their size. From V_{15} (radius = 0.35 nm), the positron annihilation characteristics start to converge, with a concentration higher to 10^{26} m^{-3}. The corresponding $\boldsymbol{S/S_L}$ value is close to 1.35. In the case of V_1 (radius = 0.139 nm), the sensitive range of concentration is between about 5×10^{23} m^{-3} and 8×10^{23} m^{-3}, and the optimal resolution ranges from 3×10^{23} m^{-3} to 3×10^{25} m^{-3}, and the $\boldsymbol{S/S_L}$ equals 1.136 also equals to $\boldsymbol{S_{Vi}/S_L}$. For the vacancy size superior to V_{27} (radius = 0.47 nm), its lower detection limit is about 5×10^{26} m^{-3} and upper limit delcliens to 8×10^{23} m^{-3}, respectively. The most sensitive concentration range is between 5×10^{21} and 5×10^{23} m^{-3}, and the $\boldsymbol{S/S_L}$ attains 1.32.

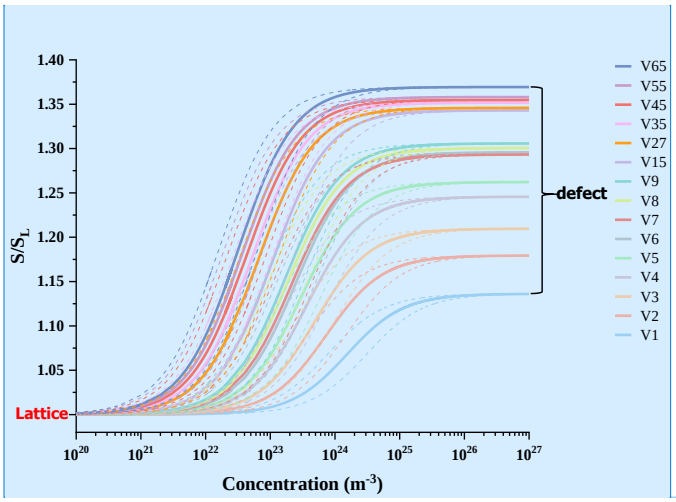

524

525 *Fig. 7: Sensitivity of PAS for each vacancy cluster in Mo using a one-trap trapping model, to be safe, the error bar (shown in*
526 *dashed line) on the concentrations was set from the uncertainty of the specific trapping coefficient from [55]*

527 Table.3 compares the calculated positron lifetime in various annihilation states from Lattice to
528 a cluster containing 65 V1s. For each state, the lifetime is analogous, particularly when a cluster
529 contains more than 8 V1s.

530 *Table 3: Calculated positron annihilation lifetime in the lattice and vacancies in W and Mo using LDA*

Annihilation state	Positron Lifetime (ps)	
	W	Mo
Lattice	101	106
V1	195	205
V2	214	223
V3	233	238
V4	261	265
V5	276	282
V6	299	303
V7	306	310
V8	312	314
V9	323	325
V15	374	375
V27	402	403
V35	413	414
V45	420	420
V55	424	425
V65	428	428

Commented [MB1]: We have to discuss about the usefulness of this figure and the associated discussion

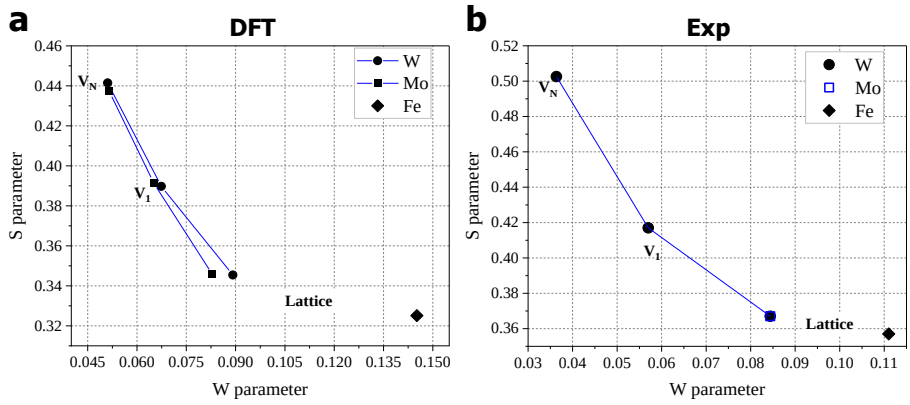

Fig. 8: a) Comparison of theortical S-W values of Lattice, V_1, and V_N for W, Mo, and Fe calculated using two-component DFT [41], b) experimental annihilation characteristics of Lattice in W and Fe [89], and V_1 and V_N in W [33,64].

Fig.9 compares the lattice annihilation characteristics of W, Mo, and Fe, using the values of ***S*** and ***W*** of V_1, V_N, and lattice determined in W as reference coordinates. The experimental results show that the difference on the annihilation characteristics of the ***Lattice*** of Fe and W are less pronounced than theoretical values. And it is then consider that the ***S, W*** of Mo and W is not disginguishable.

III. Proportion of vacancies in self-ion irradiated W

Fig. 9 represents the vacancy proportion in self-ion irradiated W with a scope of damage levels ranging from 0.0085 dpa to 1.7 dpa [9]. The V_1 was also the dominant defect at the lowest damage level.

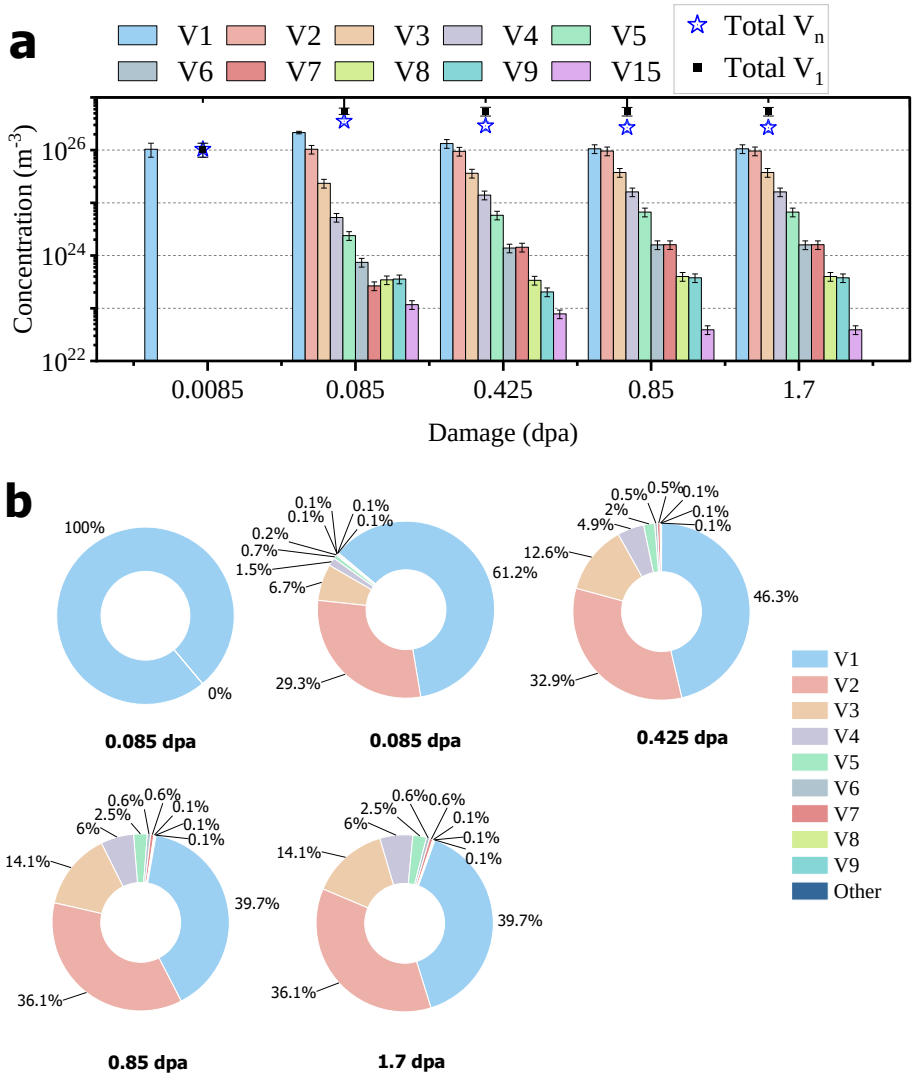

Fig. 9: a) concentration and b) proportion of the vacancy defects probed by positrons in 2 MeV self-ion [9], RT-irradiated W at first ~300 nm for damage levels ranging from 0.0085 to 1.7 dpa (with TDE= 55 eV, SRIM2008-K-P)

References

[1] T. Hirai, S. Panayotis, V. Barabash, C. Amzallag, F. Escourbiac, A. Durocher, M. Merola, J. Linke, Th. Loewenhoff, G. Pintsuk, M. Wirtz, I. Uytdenhouwen, Use of tungsten material for the ITER divertor, Nuclear Materials and Energy 9 (2016) 616–622. https://doi.org/10.1016/j.nme.2016.07.003.

[2] T. Hirai, F. Escourbiac, V. Barabash, A. Durocher, A. Fedosov, L. Ferrand, T. Jokinen, V. Komarov, M. Merola, S. Carpentier-Chouchana, N. Arkhipov, V. Kuznetcov, A. Volodin, S. Suzuki, K. Ezato, Y. Seki, B. Riccardi, M. Bednarek, P. Gavila, Status of technology R&D for the ITER tungsten divertor monoblock, Journal of Nuclear Materials 463 (2015) 1248–1251. https://doi.org/10.1016/j.jnucmat.2014.12.027.

[3] J.N. Brooks, L. El-Guebaly, A. Hassanein, T. Sizyuk, Plasma-facing material alternatives to tungsten, Nucl. Fusion 55 (2015) 043002. https://doi.org/10.1088/0029-5515/55/4/043002.

[4] A. Litnovsky, V.S. Voitsenya, R. Reichle, M. Walsh, A. Razdobarin, A. Dmitriev, N. Babinov, L. Marot, L. Moser, R. Yan, M. Rubel, A. Widdowson, S. Moon, S.G. Oh, Y. An, P. Shigin, I. Orlovskiy, K.Yu. Vukolov, E. Andreenko, A. Krimmer, V. Kotov, Ph. Mertens, Specialists Working Group on First Mirrors of the ITPA Topical Group on Diagnostics, Diagnostic mirrors for ITER: research in the frame of International Tokamak Physics Activity, Nucl. Fusion 59 (2019) 066029. https://doi.org/10.1088/1741-4326/ab1446.

[5] M. Rubel, S. Moon, P. Petersson, A. Widdowson, R.A. Pitts, S. Aleiferis, E. Fortuna-Zaleśna, G. De Temmerman, R. Reichle, First mirror erosion–deposition studies in JET using an ITER-like mirror test assembly, Nucl. Fusion 61 (2021) 046022. https://doi.org/10.1088/1741-4326/abdb92.

[6] G. Lee, C. Manière, J. McKittrick, R. Doerner, D. Nishijima, A. Gattuso, T. Abrams, D. Thomas, C. Back, E.A. Olevsky, Consolidation of Molybdenum nanopowders by spark plasma sintering: Densification mechanism and first mirror application, Journal of Nuclear Materials 516 (2019) 354–359. https://doi.org/10.1016/j.jnucmat.2019.01.028.

[7] M. Miyamoto, H. Takaoka, K. Ono, S. Morito, N. Yoshida, H. Watanabe, A. Sagara, Crystal orientation dependence of surface modification in molybdenum mirror irradiated with helium ions, Journal of Nuclear Materials 455 (2014) 297–300. https://doi.org/10.1016/j.jnucmat.2014.06.030.

[8] M.Yu. Lavrentiev, A. Hollingsworth, J. Hess, S. Davies, A. Wohlers, B. Thomas, H. Salter, A. Baron-Wiechec, I. Jepu, Y. Zayachuk, N. Peng, Effects of self-irradiation on deuterium retention and reflectivity of molybdenum, fusion plasma-facing material: Combined experimental and modeling study, Journal of Applied Physics 132 (2022) 125902. https://doi.org/10.1063/5.0099051.

[9] A. Hollingsworth, M.-F. Barthe, M.Y. Lavrentiev, P.M. Derlet, S.L. Dudarev, D.R. Mason, Z. Hu, P. Desgardin, J. Hess, S. Davies, B. Thomas, H. Salter, E.F.J. Shelton, K. Heinola, K. Mizohata, A. De Backer, A. Baron-Wiechec, I. Jepu, Y. Zayachuk, A. Widdowson, E. Meslin, A. Morellec, Comparative study of deuterium retention and vacancy content of self-ion irradiated tungsten, Journal of Nuclear Materials 558 (2022) 153373. https://doi.org/10.1016/j.jnucmat.2021.153373.

[10] P.M. Derlet, S.L. Dudarev, Microscopic structure of a heavily irradiated material, Phys. Rev. Materials 4 (2020) 023605. https://doi.org/10.1103/PhysRevMaterials.4.023605.

[11] S. Wang, W. Guo, T. Schwarz-Selinger, Y. Yuan, L. Ge, L. Cheng, X. Zhang, X. Cao, E. Fu, G.-H. Lu, Dynamic equilibrium of displacement damage defects in heavy-ion irradiated tungsten, Acta Materialia 244 (2023) 118578. https://doi.org/10.1016/j.actamat.2022.118578.

[12] S.J. Zinkle, B.N. Singh, Analysis of displacement damage and defect production under cascade damage conditions, Journal of Nuclear Materials 199 (1993) 173–191. https://doi.org/10.1016/0022-3115(93)90140-T.

[13] S. Agarwal, M.O. Liedke, A.C.L. Jones, E. Reed, A.A. Kohnert, B.P. Uberuaga, Y.Q. Wang, J. Cooper, D. Kaoumi, N. Li, R. Auguste, P. Hosemann, L. Capolungo, D.J. Edwards, M. Butterling, E.

Hirschmann, A. Wagner, F.A. Selim, A new mechanism for void-cascade interaction from nondestructive depth-resolved atomic-scale measurements of ion irradiation–induced defects in Fe, Science Advances 6 (2020) eaba8437. https://doi.org/10.1126/sciadv.aba8437.
[14] Y.-W. You, J. Sun, X.-S. Kong, X. Wu, Y. Xu, X.P. Wang, Q.F. Fang, C.S. Liu, Effects of self-interstitial atom on behaviors of hydrogen and helium in tungsten, Phys. Scr. 95 (2020) 075708. https://doi.org/10.1088/1402-4896/ab93e5.
[15] R.-Y. Zheng, W.-R. Jian, I.J. Beyerlein, W.-Z. Han, Atomic-Scale Hidden Point-Defect Complexes Induce Ultrahigh-Irradiation Hardening in Tungsten, Nano Lett. (2021) acs.nanolett.1c01637. https://doi.org/10.1021/acs.nanolett.1c01637.
[16] X.-S. Kong, Y.-W. You, Q.F. Fang, C.S. Liu, J.-L. Chen, G.-N. Luo, B.C. Pan, Z. Wang, The role of impurity oxygen in hydrogen bubble nucleation in tungsten, Journal of Nuclear Materials 433 (2013) 357–363. https://doi.org/10.1016/j.jnucmat.2012.10.024.
[17] Y.-W. You, X.-S. Kong, X.-B. Wu, C.S. Liu, Q.F. Fang, J.L. Chen, G.-N. Luo, Interaction of carbon, nitrogen and oxygen with vacancies and solutes in tungsten, RSC Adv. 5 (2015) 23261–23270. https://doi.org/10.1039/C4RA13854F.
[18] C. Song, J. Hou, L. Chen, C.S. Liu, X.-S. Kong, Bridging the gap between theory and experiment in vacancy concentration, C/N/O diffusivity, and divacancy interaction in tungsten: Role of vacancy-C/N/O interaction, Acta Materialia 263 (2024) 119516. https://doi.org/10.1016/j.actamat.2023.119516.
[19] Z. Hu, Q. Yang, F. Jomard, P. Desgardin, C. Genevois, J. Joseph, P. Olsson, T. Jourdan, M.-F. Barthe, Revealing the role of oxygen on the defect evolution of electron-irradiated tungsten: A combined experimental and simulation study, Journal of Nuclear Materials 602 (2024) 155353. https://doi.org/10.1016/j.jnucmat.2024.155353.
[20] G.-H. Lu, H.-B. Zhou, C.S. Becquart, A review of modelling and simulation of hydrogen behaviour in tungsten at different scales, Nucl. Fusion 54 (2014) 086001. https://doi.org/10.1088/0029-5515/54/8/086001.
[21] M.Y. Ye, H. Kanehara, S. Fukuta, N. Ohno, S. Takamura, Blister formation on tungsten surface under low energy and high flux hydrogen plasma irradiation in NAGDIS-I, Journal of Nuclear Materials 313–316 (2003) 72–76. https://doi.org/10.1016/S0022-3115(02)01349-1.
[22] Y. Ueda, T. Shimada, M. Nishikawa, Impacts of carbon impurities in hydrogen plasmas on tungsten blistering, Nucl. Fusion 44 (2003) 62–67. https://doi.org/10.1088/0029-5515/44/1/007.
[23] W.M. Shu, G.-N. Luo, T. Yamanishi, Mechanisms of retention and blistering in near-surface region of tungsten exposed to high flux deuterium plasmas of tens of eV, Journal of Nuclear Materials 367–370 (2007) 1463–1467. https://doi.org/10.1016/j.jnucmat.2007.04.005.
[24] D. Nishijima, M.Y. Ye, N. Ohno, S. Takamura, Formation mechanism of bubbles and holes on tungsten surface with low-energy and high-flux helium plasma irradiation in NAGDIS-II, Journal of Nuclear Materials 329–333 (2004) 1029–1033. https://doi.org/10.1016/j.jnucmat.2004.04.129.
[25] J. Zhao, X. Meng, X. Guan, Q. Wang, K. Fang, X. Xu, Y. Lu, J. Gao, Z. Liu, T. Wang, Investigation of hydrogen bubbles behavior in tungsten by high-flux hydrogen implantation, Journal of Nuclear Materials 503 (2018) 198–204. https://doi.org/10.1016/j.jnucmat.2018.03.004.
[26] E. Bernard, R. Sakamoto, E. Hodille, A. Kreter, E. Autissier, M.-F. Barthe, P. Desgardin, T. Schwarz-Selinger, V. Burwitz, S. Feuillastre, S. Garcia-Argote, G. Pieters, B. Rousseau, M. Ialovega, R. Bisson, F. Ghiorghiu, C. Corr, M. Thompson, R. Doerner, S. Markelj, H. Yamada, N. Yoshida, C. Grisolia, Tritium retention in W plasma-facing materials: Impact of the material structure and helium irradiation, Nuclear Materials and Energy 19 (2019) 403–410. https://doi.org/10.1016/j.nme.2019.03.005.
[27] A.A. Haasz, M. Poon, J.W. Davis, The effect of ion damage on deuterium trapping in tungsten, Journal of Nuclear Materials (1999) 6.
[28] Y. Ueda, H.Y. Peng, H.T. Lee, N. Ohno, S. Kajita, N. Yoshida, R. Doerner, G. De Temmerman, V. Alimov, G. Wright, Helium effects on tungsten surface morphology and deuterium retention,

650 Journal of Nuclear Materials 442 (2013) S267–S272.
651 https://doi.org/10.1016/j.jnucmat.2012.10.023.
652 [29] H. Iwakiri, K. Yasunaga, K. Morishita, N. Yoshida, Microstructure evolution in tungsten during
653 low-energy helium ion irradiation, Journal of Nuclear Materials 283–287 (2000) 1134–1138.
654 https://doi.org/10.1016/S0022-3115(00)00289-0.
655 [30] S. Kajita, W. Sakaguchi, N. Ohno, N. Yoshida, T. Saeki, Formation process of tungsten
656 nanostructure by the exposure to helium plasma under fusion relevant plasma conditions, Nucl.
657 Fusion 49 (2009) 095005. https://doi.org/10.1088/0029-5515/49/9/095005.
658 [31] J.R. Fransens, M.S.A.E. Keriem, F. Pleiter, Hydrogen-vacancy interaction in tungsten, J. Phys.:
659 Condens. Matter 3 (1991) 9871–9886. https://doi.org/10.1088/0953-8984/3/49/004.
660 [32] M.S.A.E. Keriem, D.P. van der Werf, F. Pleiter, Hydrogen-vacancy interaction in molybdenum, J.
661 Phys.: Condens. Matter 5 (1993) 1801. https://doi.org/10.1088/0953-8984/5/12/008.
662 [33] P.E. Lhuillier, M.F. Barthe, P. Desgardin, W. Egger, P. Sperr, Positron annihilation studies on the
663 nature and thermal behaviour of irradiation induced defects in tungsten, Phys. Status Solidi (c) 6
664 (2009) 2329–2332. https://doi.org/10.1002/pssc.200982114.
665 [34] P.-E. Lhuillier, Etude du comportement de l'hélium et des défauts lacunaires dans le tungstène,
666 phdthesis, Université d'Orléans, 2010. https://tel.archives-ouvertes.fr/tel-00587482 (accessed
667 January 7, 2021).
668 [35] A. Debelle, M.F. Barthe, T. Sauvage, First temperature stage evolution of irradiation-induced
669 defects in tungsten studied by positron annihilation spectroscopy, Journal of Nuclear Materials
670 376 (2008) 216–221. https://doi.org/10.1016/j.jnucmat.2008.03.002.
671 [36] Hautojärvi, Corbel C., Positron Spectroscopy of Defects in Metals and Semiconductors, ENFI 125
672 (1995) 491–532. https://doi.org/10.3254/978-1-61499-211-0-491.
673 [37] M. Hakala, M.J. Puska, R.M. Nieminen, Momentum distributions of electron-positron pairs
674 annihilating at vacancy clusters in Si, Phys. Rev. B 57 (1998) 7621–7627.
675 https://doi.org/10.1103/PhysRevB.57.7621.
676 [38] M.J. Puska, R.M. Nieminent, Defect spectroscopy with positrons: a general calculational method,
677 (n.d.) 15.
678 [39] Q. Yang, X. Cao, B. Wang, P. Wang, P. Olsson, Systematic investigation of positron annihilation in
679 transition metals from first principles, Phys. Rev. B 108 (2023) 104113.
680 https://doi.org/10.1103/PhysRevB.108.104113.
681 [40] I. Makkonen, M. Hakala, M.J. Puska, Modeling the momentum distributions of annihilating
682 electron-positron pairs in solids, Phys. Rev. B 73 (2006) 035103.
683 https://doi.org/10.1103/PhysRevB.73.035103.
684 [41] Q. Yang, Z. Hu, I. Makkonen, P. Desgardin, W. Egger, M.-F. Barthe, P. Olsson, A combined
685 experimental and theoretical study of small and large vacancy clusters in tungsten, Journal of
686 Nuclear Materials 571 (2022) 154019. https://doi.org/10.1016/j.jnucmat.2022.154019.
687 [42] Z. Hu, J. Wu, Q. Yang, F. Jomard, F. Granberg, M.-F. Barthe, New Insight into the Quantifying
688 Vacancy Distribution in Self-Ion-Irradiated Tungsten: A Combined Experimental and
689 Computational Study, Nano Lett. (2025). https://doi.org/10.1021/acs.nanolett.5c01711.
690 [43] J. Hou, X.-S. Kong, W. Hu, H. Deng, D. Nguyen-Manh, J. Song, Deuterium Trapping and Desorption
691 by Vacancy Clusters in Irradiated Mo from Object Kinetic Monte Carlo Simulations, (2024).
692 https://doi.org/10.2139/ssrn.4700194.
693 [44] R.E. Stoller, M.B. Toloczko, G.S. Was, A.G. Certain, S. Dwaraknath, F.A. Garner, On the use of
694 SRIM for computing radiation damage exposure, Nuclear Instruments and Methods in Physics
695 Research Section B: Beam Interactions with Materials and Atoms 310 (2013) 75–80.
696 https://doi.org/10.1016/j.nimb.2013.05.008.
697 [45] Y.-R. Lin, S.J. Zinkle, C.J. Ortiz, J.-P. Crocombette, R. Webb, R.E. Stoller, Predicting displacement
698 damage for ion irradiation: Origin of the overestimation of vacancy production in SRIM full-
699 cascade calculations, Current Opinion in Solid State and Materials Science 27 (2023) 101120.
700 https://doi.org/10.1016/j.cossms.2023.101120.

[46] P. Jung, G. Lucki, Damage production by fast electrons in dilute alloys of vanadium, niobium and molybdenum, Radiation Effects 26 (1975) 99–103. https://doi.org/10.1080/00337577508237426.
[47] P. Desgardin, L. Liszkay, M.F. Barthe, L. Henry, J. Briaud, M. Saillard, L. Lepolotec, C. Corbel, G. Blondiaux, A. Colder, P. Marie, M. Levalois, Slow Positron Beam Facility in Orléans, MSF 363–365 (2001) 523–525. https://doi.org/10.4028/www.scientific.net/MSF.363-365.523.
[48] E. Soininen, H. Huomo, P.A. Huttunen, J. Mäkinen, A. Vehanen, P. Hautojärvi, Temperature dependence of positron diffusion in cubic metals, Phys. Rev. B 41 (1990) 6227–6233. https://doi.org/10.1103/PhysRevB.41.6227.
[49] A. van Veen, H. Schut, J. de Vries, R.A. Hakvoort, M.R. Ijpma, Analysis of positron profiling data by means of '"VEPFIT,"' in: AIP Conference Proceedings, AIP, Ontario (Canada), 1991: pp. 171–198. https://doi.org/10.1063/1.40182.
[50] A. van Veen, H. Schut, M. Clement, J.M.M. de Nijs, A. Kruseman, M.R. IJpma, VEPFIT applied to depth profiling problems, Applied Surface Science 85 (1995) 216–224. https://doi.org/10.1016/0169-4332(94)00334-3.
[51] P.J. Schultz, K.G. Lynn, Interaction of positron beams with surfaces, thin films, and interfaces, Rev. Mod. Phys. 60 (1988) 701–779. https://doi.org/10.1103/RevModPhys.60.701.
[52] R.S. Brusa, W. Deng, G.P. Karwasz, A. Zecca, Doppler-broadening measurements of positron annihilation with high-momentum electrons in pure elements, Nuclear Instruments and Methods in Physics Research Section B: Beam Interactions with Materials and Atoms 194 (2002) 519–531. https://doi.org/10.1016/S0168-583X(02)00953-9.
[53] Z. Hu, Q. Yang, F. Jomard, P. Desgardin, C. Genevois, J. Joseph, P. Olsson, T. Jourdan, M.-F. Barthe, Revealing the role of oxygen on the defect evolution of electron-irradiated tungsten: A combined experimental and simulation study, Journal of Nuclear Materials 602 (2024) 155353. https://doi.org/10.1016/j.jnucmat.2024.155353.
[54] Z. Hu, P. Desgardin, C. Genevois, J. Joseph, B. Décamps, R. Schäublin, M.-F. Barthe, Effect of purity on the vacancy defects induced in self–irradiated tungsten: A combination of PAS and TEM, Journal of Nuclear Materials 556 (2021) 153175. https://doi.org/10.1016/j.jnucmat.2021.153175.
[55] Z. Hu, J. Wu, F. Jomard, F. Granberg, M.-F. Barthe, New insight into quantifying vacancy distribution in self-ion irradiated tungsten: a combined experimental and computational study, (2024). https://doi.org/10.48550/arXiv.2411.13480.
[56] G. Kresse, J. Furthmüller, Efficient iterative schemes for ab initio total-energy calculations using a plane-wave basis set, Phys. Rev. B 54 (1996) 11169–11186. https://doi.org/10.1103/PhysRevB.54.11169.
[57] P.E. Blöchl, Projector augmented-wave method, Phys. Rev. B 50 (1994) 17953–17979. https://doi.org/10.1103/PhysRevB.50.17953.
[58] J.P. Perdew, K. Burke, M. Ernzerhof, Generalized Gradient Approximation Made Simple, Phys. Rev. Lett. 77 (1996) 3865–3868. https://doi.org/10.1103/PhysRevLett.77.3865.
[59] J. Hou, Y.-W. You, X.-S. Kong, J. Song, C.S. Liu, Accurate prediction of vacancy cluster structures and energetics in bcc transition metals, Acta Materialia 211 (2021) 116860. https://doi.org/10.1016/j.actamat.2021.116860.
[60] E. Boroński, R.M. Nieminen, Electron-positron density-functional theory, Phys. Rev. B 34 (1986) 3820–3831. https://doi.org/10.1103/PhysRevB.34.3820.
[61] A. Rubaszek, Electron-positron enhancement factors at a metal surface: Aluminum, Phys. Rev. B 44 (1991) 10857–10868. https://doi.org/10.1103/PhysRevB.44.10857.
[62] V. Callewaert, R. Saniz, B. Barbiellini, A. Bansil, B. Partoens, Application of the weighted-density approximation to the accurate description of electron-positron correlation effects in materials, Phys. Rev. B 96 (2017) 085135. https://doi.org/10.1103/PhysRevB.96.085135.
[63] M. Alatalo, B. Barbiellini, M. Hakala, H. Kauppinen, T. Korhonen, M.J. Puska, K. Saarinen, P. Hautojärvi, R.M. Nieminen, Theoretical and experimental study of positron annihilation with

core electrons in solids, Phys. Rev. B 54 (1996) 2397–2409. https://doi.org/10.1103/PhysRevB.54.2397.
[64] M. Sidibe, Etude du comportement du tungstène sous irradiation : applications aux réacteurs de fusion, phdthesis, Université d'Orléans, 2014. https://tel.archives-ouvertes.fr/tel-01068634 (accessed January 7, 2021).
[65] C. He, Experimental study of the interaction of vacancy defects with Y, O and Ti solutes to better understand their roles in the nanoparticles formation in ODS steels, These de doctorat, Orléans, 2014. http://www.theses.fr/2014ORLE2057 (accessed January 17, 2021).
[66] F. Granberg, J. Byggmästar, K. Nordlund, Molecular dynamics simulations of high-dose damage production and defect evolution in tungsten, Journal of Nuclear Materials 556 (2021) 153158. https://doi.org/10.1016/j.jnucmat.2021.153158.
[67] A.P. Selby, D. Xu, N. Juslin, N.A. Capps, B.D. Wirth, Primary defect production by high energy displacement cascades in molybdenum, Journal of Nuclear Materials 437 (2013) 19–23. https://doi.org/10.1016/j.jnucmat.2013.01.332.
[68] J. Hou, X. Kong, W. Hu, H. Deng, D. Nguyen-Manh, J. Song, Deuterium trapping and desorption by vacancy clusters in irradiated Mo from object kinetic Monte Carlo simulations, Acta Materialia 274 (2024) 120014. https://doi.org/10.1016/j.actamat.2024.120014.
[69] Z. Hu, L'effet de la pureté sur l'évolution de la microstructure du tungstène sous irradiation, Http://Www.Theses.Fr (2022). http://www.theses.fr/s265136 (accessed September 15, 2022).
[70] B. Wieluńska-Kuś, M. Dickmann, W. Egger, M. Zibrov, Ł. Ciupiński, Positron lifetime study of ion-irradiated tungsten: Ion type and dose effects, Nuclear Materials and Energy (2024) 101610. https://doi.org/10.1016/j.nme.2024.101610.
[71] L. Ventelon, F. Willaime, C.-C. Fu, M. Heran, I. Ginoux, Ab initio investigation of radiation defects in tungsten: Structure of self-interstitials and specificity of di-vacancies compared to other bcc transition metals, Journal of Nuclear Materials 425 (2012) 16–21. https://doi.org/10.1016/j.jnucmat.2011.08.024.
[72] M. Muzyk, D. Nguyen-Manh, K.J. Kurzydłowski, N.L. Baluc, S.L. Dudarev, Phase stability, point defects, and elastic properties of W-V and W-Ta alloys, Phys. Rev. B 84 (2011) 104115. https://doi.org/10.1103/PhysRevB.84.104115.
[73] C.S. Becquart, C. Domain, Ab initio calculations about intrinsic point defects and He in W, Nuclear Instruments and Methods in Physics Research Section B: Beam Interactions with Materials and Atoms 255 (2007) 23–26. https://doi.org/10.1016/j.nimb.2006.11.006.
[74] J.Y. Park, H.C.W. Huang, R.W. Siegel, R.W. Balluffi, A quantitative study of vacancy defects in quenched tungsten by combined field-ion microscopy and electrical resistometry, Philosophical Magazine A 48 (1983) 397–419. https://doi.org/10.1080/01418618308234901.
[75] C.S. Becquart, C. Domain, U. Sarkar, A. DeBacker, M. Hou, Microstructural evolution of irradiated tungsten: Ab initio parameterisation of an OKMC model, Journal of Nuclear Materials 403 (2010) 75–88. https://doi.org/10.1016/j.jnucmat.2010.06.003.
[76] K. Heinola, F. Djurabekova, T. Ahlgren, On the stability and mobility of di-vacancies in tungsten, Nucl. Fusion 58 (2018) 026004. https://doi.org/10.1088/1741-4326/aa99ee.
[77] A. Zhong, C. Lapointe, A.M. Goryaeva, K. Arakawa, M. Athènes, M.-C. Marinica, Unraveling Temperature-Induced Vacancy Clustering in Tungsten: From Direct Microscopy to Atomistic Insights via Data-Driven Bayesian Sampling, PRX Energy 4 (2025) 013008. https://doi.org/10.1103/PRXEnergy.4.013008.
[78] P.-W. Ma, S.L. Dudarev, Symmetry-broken self-interstitial defects in chromium, molybdenum, and tungsten, Phys. Rev. Materials 3 (2019) 043606. https://doi.org/10.1103/PhysRevMaterials.3.043606.
[79] A. De Backer, C. Domain, C.S. Becquart, L. Luneville, D. Simeone, A.E. Sand, K. Nordlund, A model of defect cluster creation in fragmented cascades in metals based on morphological analysis, J. Phys.: Condens. Matter 30 (2018) 405701. https://doi.org/10.1088/1361-648X/aadb4e.

[80] A. Fellman, A.E. Sand, J. Byggmästar, K. Nordlund, Radiation damage in tungsten from cascade overlap with voids and vacancy clusters, J. Phys.: Condens. Matter 31 (2019) 405402. https://doi.org/10.1088/1361-648X/ab2ea4.
[81] F. Granberg, J. Byggmästar, K. Nordlund, Cascade overlap with vacancy-type defects in Fe, Eur. Phys. J. B 92 (2019) 146. https://doi.org/10.1140/epjb/e2019-100240-3.
[82] K. Nordlund, S.J. Zinkle, A.E. Sand, F. Granberg, R.S. Averback, R. Stoller, T. Suzudo, L. Malerba, F. Banhart, W.J. Weber, F. Willaime, S.L. Dudarev, D. Simeone, Improving atomic displacement and replacement calculations with physically realistic damage models, Nat Commun 9 (2018) 1084. https://doi.org/10.1038/s41467-018-03415-5.
[83] A.Yu. Konobeyev, U. Fischer, Yu.A. Korovin, S.P. Simakov, Evaluation of effective threshold displacement energies and other data required for the calculation of advanced atomic displacement cross-sections, Nuclear Energy and Technology 3 (2017) 169–175. https://doi.org/10.1016/j.nucet.2017.08.007.
[84] R. Pasianot, M. Alurralde, A. Almazouzi, M. Victoria, Primary damage formation in molybdenum: A computer simulation study, Philosophical Magazine A 82 (2002) 1671–1689. https://doi.org/10.1080/01418610208235683.
[85] Primary Radiation Damage in Materials, Nuclear Energy Agency (NEA) (n.d.). https://www.oecd-nea.org/jcms/pl_19620/primary-radiation-damage-in-materials?details=true (accessed October 10, 2023).
[86] D.R. Mason, S. Das, P.M. Derlet, S.L. Dudarev, A.J. London, H. Yu, N.W. Phillips, D. Yang, K. Mizohata, R. Xu, F. Hofmann, Observation of Transient and Asymptotic Driven Structural States of Tungsten Exposed to Radiation, Phys. Rev. Lett. 125 (2020) 225503. https://doi.org/10.1103/PhysRevLett.125.225503.
[87] Q. Yang, P. Olsson, Full energy range primary radiation damage model, Phys. Rev. Materials 5 (2021) 073602. https://doi.org/10.1103/PhysRevMaterials.5.073602.
[88] R.H.J. Fastenau, L.M. Caspers, A. van Veen, Small clusters of vacancies and helium in molybdenum, Phys. Stat. Sol. (a) 34 (1976) 277–289. https://doi.org/10.1002/pssa.2210340124.
[89] W. Asplet, Etude des interactions entre les défauts lacunaires et les solutés Y,O, Ti pour mieux comprendre leur rôle dans la formation des nanoparticules d'oxydes dans les aciers ODS, (n.d.) 269.